nature materials

LETTERS

PUBLISHED ONLINE: 13 DECEMBER 2009 | DOI: 10.1038/NMAT2609

Aharonov–Bohm interference in topological insulator nanoribbons

Hailin Peng[1,2]*, Keji Lai[3,4]*, Desheng Kong[1], Stefan Meister[1], Yulin Chen[3,4,5], Xiao-Liang Qi[4,5], Shou-Cheng Zhang[4,5], Zhi-Xun Shen[3,4,5] and Yi Cui[1]†

Topological insulators represent unusual phases of quantum matter with an insulating bulk gap and gapless edges or surface states. The two-dimensional topological insulator phase was predicted in HgTe quantum wells[1] and confirmed by transport measurements[2]. Recently, Bi_2Se_3 and related materials have been proposed as three-dimensional topological insulators with a single Dirac cone on the surface[3,4], protected by time-reversal symmetry[5–7]. The topological surface states have been observed by angle-resolved photoemission spectroscopy experiments[4,8]. However, few transport measurements[9] in this context have been reported, presumably owing to the predominance of bulk carriers from crystal defects or thermal excitations[10]. Here we show unambiguous transport evidence of topological surface states through periodic quantum interference effects in layered single-crystalline Bi_2Se_3 nanoribbons, which have larger surface-to-volume ratios than bulk materials and can therefore manifest surface effects. Pronounced Aharonov–Bohm oscillations[11] in the magnetoresistance clearly demonstrate the coherent propagation of two-dimensional electrons around the perimeter of the nanoribbon surface, as expected from the topological nature of the surface states. The dominance of the primary *h/e* oscillation, where *h* is Planck's constant and *e* is the electron charge, and its temperature dependence demonstrate the robustness of these states. Our results suggest that topological insulator nanoribbons afford promising materials for future spintronic devices at room temperature[12].

Electronic properties at the surface of a solid can be very different from those in the bulk. Dangling bonds or reconstruction of the atoms owing to the inevitable loss of periodic lattice structure could result in surface states, which are absent in the bulk energy spectrum. In most materials, details of the surface geometry and chemistry can easily alter these fragile states. Recent theoretical work, however, has predicted a new class of quantum matter with an insulating bulk gap and gapless edge or surface states: the topological insulators in two[1,13,14] and three dimensions[5–7], respectively. These robust low-dimensional conducting states are topologically protected against all time-reversal-invariant perturbations, such as scattering by non-magnetic impurities, crystalline defects and distortion of the surface itself. Dissipationless spin currents may be generated at the edge or surface states for spintronics and quantum-computing applications. Experimentally, the two-dimensional (2D) topological insulator phase has been predicted and realized in HgTe quantum wells[1,2]. The 3D topological insulator phase was reported in $Bi_{1-x}Sb_x$ alloy[15] with complicated topological surface states. 3D topological insulators with the simplest possible surface states consisting of a single Dirac cone, on the other hand, have been proposed theoretically[3] in stoichiometric compounds Bi_2Se_3, Bi_2Te_3 and Sb_2Te_3, and topological surface states have been observed independently by angle-resolved photoemission spectroscopy (ARPES) experiments in Bi_2Se_3 (ref. 4). Recently, the bulk insulating phase has been achieved in Bi_2Te_3 (ref. 8) as observed by ARPES. Among these materials, Bi_2Se_3, a narrow gap semiconductor for infrared detectors and thermoelectric applications[16], has a simple band structure with a single Dirac cone on the surface and a large non-trivial bulk gap of 0.3 eV (refs 3, 4). These properties make Bi_2Se_3 ideal for the realization of interesting topological phenomena, such as the image monopole effect[7,17] and Majorana fermions[18], as well as future room-temperature spintronic applications.

However, the surface states in topological insulators have been mainly investigated by ARPES (refs 4, 8, 15). Transport measurements, on the other hand, should be a straightforward probe to study the properties of such low-dimensional electronic states[10]. For instance, if conduction occurs mainly through the 2D channel, the conductance would scale with the geometry of the sample surface rather than that of the bulk. Under strong magnetic fields, the characteristics of the 2D Fermi surface can be mapped out by the Shubnikov–de Haas (SdH) oscillations of the magnetoresistance[19], in which the magnetoresistance varies periodically with the inverse magnetic field ($1/B$). Finally, quantum interference effects associated with the surface states may occur for mesoscopic samples where the low-temperature phase coherence length is comparable to the sample dimensions[20]. However, despite extensive transport experiments on bulk Bi_2Se_3 since the 1970s (ref. 21), there has been no report of a conducting surface layer, and the predicted topological features have not been addressed. Such a seeming discrepancy is understandable in a macroscopic bulk crystal because the residual bulk carriers owing to crystal defects or thermal excitations in a small bulk gap semiconductor can easily mask the transport signatures of the 2D surface electrons.

The contribution of the bulk carriers can be suppressed by reducing sample size. Quasi-1D nanoribbons, with their large surface-to-volume ratios, provide excellent geometries for probing the transport properties of surface states. In this work, single-crystalline Bi_2Se_3 nanoribbons are synthesized by means of a gold-catalysed vapour–liquid–solid (VLS) growth[22]. The layered Bi_2Se_3 has a rhombohedral phase with the space group D_{3d}^5 ($R\bar{3}m$)

[1]Department of Materials Science and Engineering, Stanford University, Stanford, California 94305, USA, [2]College of Chemistry and Molecular Engineering, Peking University, Beijing 100871, P. R. China, [3]Department of Applied Physics, Stanford University, Stanford, California 94305, USA, [4]Department of Physics, Stanford University, Stanford, California 94305, USA, [5]Stanford Institute for Materials and Energy Sciences, SLAC National Accelerator Laboratory, 2575 Sand Hill Road, Menlo Park, California 94025, USA. *These authors contributed equally to this work.
†e-mail: yicui@stanford.edu.

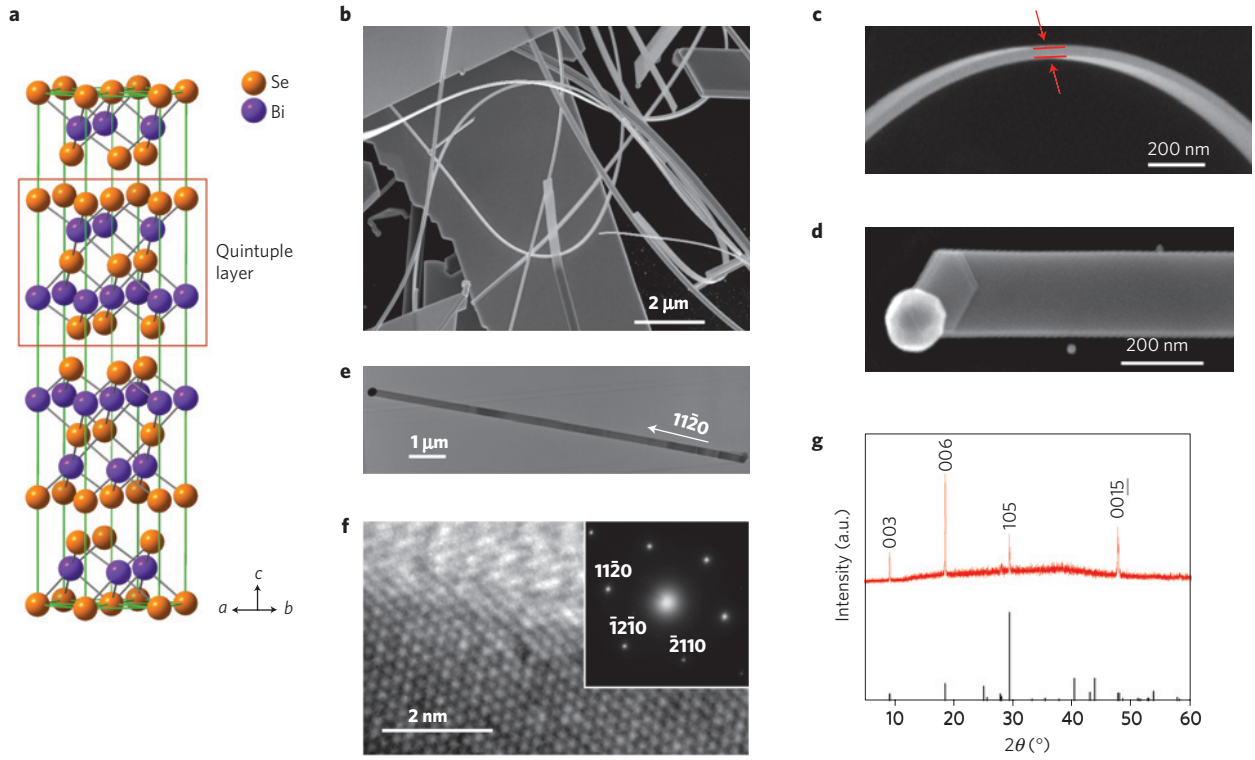

Figure 1 | Crystal structure and characterization of the Bi_2Se_3 nanoribbons. a, Layered crystal structure of Bi_2Se_3 with quintuple layers ordered in the Se–Bi–Se–Bi–Se sequence along the *c* axis. **b**, SEM image of as-grown nanoribbons from Bi_2Se_3 evaporation by VLS growth. **c**, High-resolution SEM image showing the ribbon shape and flat surfaces of a 30-nm-thick nanoribbon. **d**, Close-up view of a nanoribbon with a gold nanoparticle catalyst at the end. **e**, TEM image of a Bi_2Se_3 nanoribbon with a nanoparticle at the tip. **f**, High-resolution TEM image of the edge of the Bi_2Se_3 nanoribbon showing the smooth surfaces with little (<1 nm) amorphous layers. The selected-area electron diffraction pattern (inset) indicates that the ribbon is single-crystalline all along its length. The growth direction of the nanoribbon is along [11$\bar{2}$0]. **g**, X-ray powder diffraction pattern of Bi_2Se_3 nanoribbons with a reference diffractogram (PDF cards no. 00-033-0214). The products were identified as the single-phase rhombohedral Bi_2Se_3 ($R\bar{3}m$, $a = b = 0.4140$ nm and $c = 2.8636$ nm).

(ref. 23), and consists of planar, covalently bonded sheets linked predominantly by van der Waals interactions (Fig. 1a). Figure 1b shows a typical scanning electron microscopy (SEM) image of the as-grown Bi_2Se_3 nanoribbons with thicknesses of 25–100 nm and widths ranging from 50 nm to several micrometres. The nanoribbon has smooth side walls and flat surfaces (Fig. 1c). The presence of a gold nanoparticle at the end of each nanoribbon suggests the VLS growth mechanism, in which catalyst particles promote nucleation and unidirectional growth of layered structures (Fig. 1d,e). Energy-dispersive X-ray spectroscopy analyses reveal uniform chemical composition along the ribbon length with a Bi/Se atomic ratio of 2:3, indicating stoichiometric Bi_2Se_3 free of detectable impurities, such as gold and oxygen (Supplementary Fig. S1). The nanoribbons are single-crystalline rhombohedral phase with atomically smooth edges, length along the [11$\bar{2}$0] direction and height parallel to the *c* axis, as shown by transmission electron microscopy (TEM, Fig. 1f and Supplementary Fig. S2), the selected area electron diffraction pattern (Fig. 1f, inset) and the X-ray diffraction pattern (Fig. 1g). Scanning tunnelling microscope data (not shown) show ordered honeycomb lattices with no gold or other metal layers masking the surface. By controlling the growth temperature, using Sn/Au alloy as the catalyst, or post-annealing in Se vapour, we are able to vary the electron density without changing the crystal structure (Supplementary Figs S2 and S3). The total electron density measured by the Hall effect is between 3×10^{13} and 2×10^{14} cm^{-2}, with an effective Hall mobility $\sim 2 \times 10^3$ cm^2 V^{-1} s^{-1} extracted from the sheet resistance (Supplementary Fig. S4). Such a high electron density indicates the existence of bulk carriers in our nanoribbons, with the 3D density comparable to that observed in degenerate single crystals[21] (Supplementary Fig. S4). The contribution of bulk carriers to the total conduction, however, is suppressed compared with macroscopic samples. The results reported below are observed only in samples with relatively low total density $\sim 5 \times 10^{13}$ cm^{-2}.

The quasi-1D narrow nanoribbons in Fig. 1e are model systems for studying the topological surface states. When an external magnetic field (B) is applied along the length of the nanoribbon, quantum interference effects will occur if the conduction electrons remain phase coherent after completing closed trajectories, each encircling a certain magnetic flux. For the bulk carriers, there exist various sample-specific, or more precisely, impurity-dependent loops, resulting in universal conductance fluctuations[24] (UCFs) with aperiodic field dependence, commonly observed in small metallic and semiconducting structures. For the 2D states covering the entire surface, however, all phase-coherent trajectories participating in the quantum interference enclose the same area perpendicular to the B field (Fig. 2a). The low-temperature transport therefore shows periodic magnetoresistance oscillations, a hallmark of the well-known Aharonov–Bohm effect[11], with a characteristic period of the external magnetic field $\Delta B = \Phi_0/S$, where $\Phi_0 = h/e$ is the flux quantum, S is the cross-sectional area of the nanoribbon, h is Planck's constant and e is the electron charge.

To probe the quantum interference effect in the Bi_2Se_3 nanoribbons, we fabricated four-point probe devices by depositing Ti/Au ohmic contacts. A representative device is shown in Fig. 2b, where the width w and thickness t of the ribbon are determined by SEM and atomic force microscopy (AFM), respectively. A standard lock-in technique ($I = 0.1$–1 μA) is used to measure the four-terminal magnetoresistance in a 9 T Quantum Design PPMS system with a base temperature of 2 K. At low magnetic fields

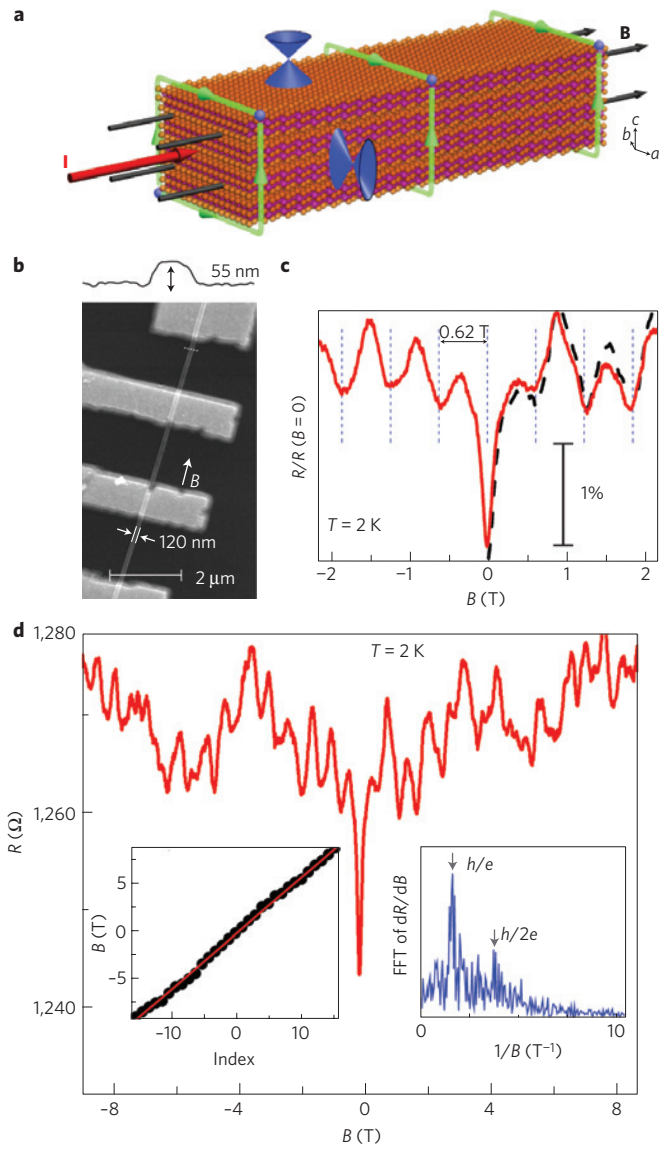

Figure 2 | Aharonov–Bohm oscillations of the topological surface states. **a**, Schematic diagram of 2D topological surface states of a layered Bi_2Se_3 nanoribbon under a magnetic field along the ribbon length. The red and black arrows correspond to the electric current and magnetic field lines, respectively. The two cones on the top and side surfaces illustrate the Dirac surface states propagating on all surfaces with linear dispersion. The green loops encircling the same magnetic flux stand for phase-coherent paths through which the surface electrons interfere. **b**, SEM image of a Bi_2Se_3 nanoribbon, 120 nm in width, contacted by four Ti/Au electrodes. The thickness of the nanoribbon is measured by AFM (a line cut in the inset) to be 55 nm. The measurement error bars from both SEM and AFM are within 5–10%. **c**, Normalized magnetoresistance of the nanoribbon in radial magnetic fields at 2 K. A clear modulation of the resistance with a period of 0.62 T is observed, corresponding to one flux quantum (h/e) threaded into the cross-section of the nanoribbon. The solid red trace (up sweep) was taken with a scan rate of 3 mT s^{-1} and the dashed black line (down sweep) at 10 mT s^{-1}. **d**, Magnetoresistance in the full field range of ±9 T. Inset on the left, magnetic field position of well-developed resistance minima. Inset on the right, FFT of the derivative dR/dB in the entire field range. Locations of h/e and $h/2e$ flux quantization are labelled.

$|B| < 0.15$ T, the weak anti-localization effect[25] with a sharp cusp at zero field is seen in Fig. 2c, consistent with the presence of strong spin–orbit coupling in Bi_2Se_3. For fields $0.15\,\text{T} < |B| < 2\,\text{T}$, pronounced and reproducible resistance oscillations with a period of 0.62 T are observed. For the h/e Aharonov–Bohm effect, this period is associated with an area of $6.7 \times 10^{-15}\,\text{m}^2$, in excellent agreement with the measured cross-sectional area of the nanoribbon $S = w \cdot t = 6.6 \times 10^{-15}\,\text{m}^2$ (Fig. 2b), given the experimental error bars in measuring both w and t. At higher fields (Fig. 2d), the perfect periodicity deteriorates slightly, but a roughly linear relation of 0.6 T per resistance minimum still holds up to ±9 T. As shown in the inset of Fig. 2d, the prominent h/e oscillation and a weak second harmonic at $h/2e$ are better seen by taking the fast Fourier transform (FFT) of the derivative dR/dB, a method commonly applied to separate the oscillatory part from slow-varying background[26]. Taking the width of the spectral peak at h/e as an estimate for the uncertainty of oscillation frequencies, we obtain an upper bound of the surface state thickness ~6 nm. The noisy background in the FFT spectrum and the deviation from pure h/e periodicity at high fields are presumably due to the contribution from the bulk states, which superimpose aperiodic UCFs onto the clean Aharonov–Bohm oscillations. We also note that SdH oscillations of the bulk electrons may be responsible for the slow-varying background seen in Fig. 2d. As quantum confinement in the plane perpendicular to the field direction is not negligible, several electric sub-bands may form in our nanoribbons, and magnetic depopulation of these sub-bands would modify the usual $1/B$ relation at high Landau level fillings[27]. Nevertheless, neither of these bulk-related effects could result in B periodicity over the large field range in this experiment. Therefore, the Aharonov–Bohm effect in Bi_2Se_3 nanoribbons indisputably manifests the existence of the conducting surface states, which, on the basis of theories and the ARPES data[3,4], are highly exotic as opposed to the trivial surface inversion effect in certain semiconducting materials.

The observation of the Aharonov–Bohm oscillations in Bi_2Se_3 nanostructures provides important insights into the topological surface states. First, although a significant portion of the conduction is carried by the bulk states, the interaction between bulk and surface electrons does not destroy the phase coherence of the surface states. The oscillation amplitude observed in our experiment is of the order of the quantized conductance (e^2/h), comparable to other quasi-1D nanostructures[26] and disordered metal cylinders[20]. As full revolution around the perimeter of the ribbon is required for the interference effect, our result demonstrates that the surface states not only exist on the top and bottom (0001) surfaces but also propagate coherently through the side walls of the nanoribbon. Given that the side surface is terminated with dangling bonds and adjacent quasi-2D layers are predominantly linked by van der Waals coupling, the coherent motion of the electrons through the side surface is highly non-trivial, providing further evidence for the topological robustness of the surface states. Finally, the primary oscillation period corresponds to the Aharonov–Bohm h/e quantization, whereas the Altshuler–Aronov–Spivak (AAS) oscillation with $h/2e$ period[28,29] originating from weak (anti) localization is suppressed. The absence of the AAS effect, at least in the low-magnetic-field region, may be related to the distinct property of the topological surface states; that is, electrons with opposite momentum have opposite spin polarization. For these states, backscattering events are forbidden for $B = 0$ but are present for finite field strengths even if the flux of the field is an integer multiple of $h/2e$ flux quanta. Consequently, the anti-localization behaviour observed at $B = 0$ is absent for other integer multiples of $h/2e$ flux, leading to the suppression of the AAS effect.

Further information about the Aharonov–Bohm effect can be obtained by the temperature evolution of the magnetoresistance oscillations. As shown in Fig. 3a, most oscillatory features persist up to 20 K, beyond which the zero field resistance increases considerably (Fig. 3b, inset), presumably owing to phonon scattering. Again, we take the FFT of dR/dB to analyse the T dependence data. In Fig. 3b,

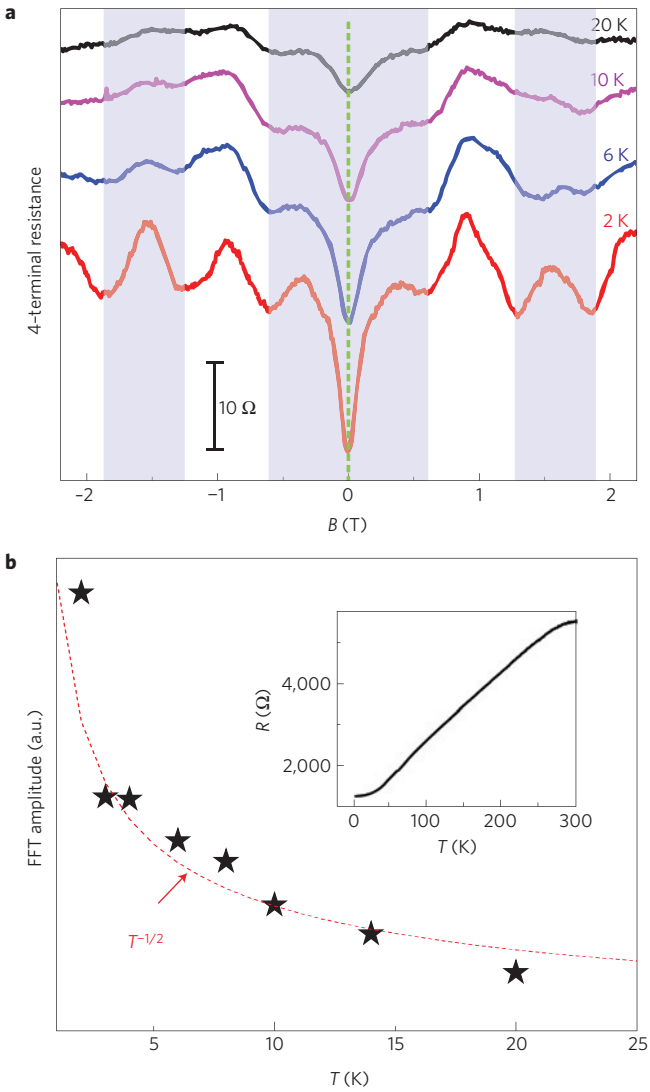

Figure 3 | Temperature dependence of the Aharonov–Bohm oscillations. **a**, Magnetoresistance versus magnetic field at four different temperatures. The curves are vertically displaced for clarity. **b**, T dependence of the FFT amplitude of the primary h/e oscillations. The data roughly follow the expected $T^{-1/2}$ relation (dashed line) between 2 and 20 K. The fitted temperature exponent is -0.6 ± 0.1 within this range. Inset: Zero field cooling curve from 300 to 2 K.

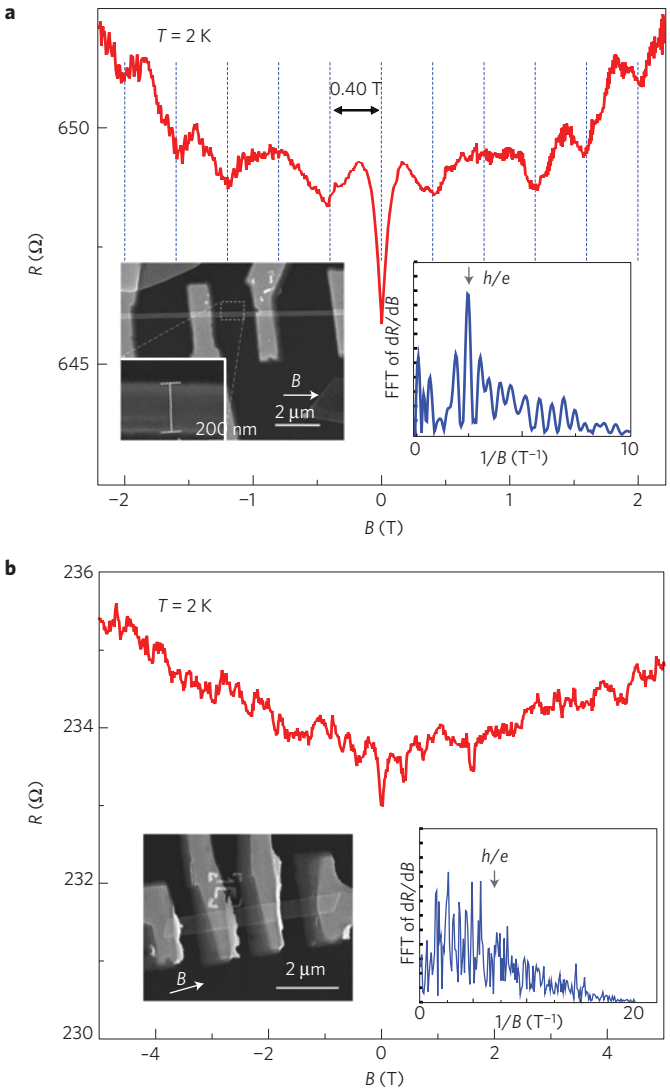

Figure 4 | Magnetoresistance of two more Bi_2Se_3 nanoribbons. **a**, Aharonov–Bohm oscillations of the nanoribbon shown in the inset. The label h/e marks the calculated (from the cross-section 200 nm × 50 nm) $1/B$ frequency in the FFT plot. **b**, Aperiodic magnetoresistance of a wide ribbon (570 nm × 50 nm) and the SEM in the inset. The FFT spectrum shows no apparent peaks. The location of h/e is again indicated for comparison.

the h/e oscillation amplitude roughly scales with $T^{-1/2}$ between 2 and 20 K, where the inelastic phonon scattering is negligible. The same T dependence was observed in mesoscopic metal rings and explained by the averaging of conduction channels in the absence of inelastic scattering[30]. At high densities with weak electron–electron interaction, the phase-breaking time τ_ϕ can be estimated from the thermal broadening of the Fermi–Dirac distribution, or $\tau_\phi \sim \hbar/k_B T$. As a result, the oscillation amplitude δR scales with the phase-coherent diffusion length $L_\phi = (D\tau_\phi)^{1/2} \sim T^{-1/2}$, where D is the diffusion constant, in accordance with the experimental data.

Finally, we briefly discuss the quantum interference effect in two more Bi_2Se_3 nanoribbon devices at 2 K. For the relatively narrow ribbon in Fig. 4a, well-defined resistance minima are observed at multiples of 0.4 T, except for weak shoulders at ±0.8 T. This period is better seen in the FFT plot. The inferred area from the h/e flux quantization again matches the cross-sectional area (200 nm × 50 nm) well within the measurement error bars. On the other hand, the magnetoresistance of the wide ribbon (570 nm × 50 nm) in Fig. 4b does not show obvious periodicity, and the characteristics of its Fourier spectrum are reminiscent of the UCF effect. In other words, neither the bulk nor the surface electrons can produce a coherent path that predominantly encloses a fixed amount of flux. Thus, the phase-coherent length L_ϕ in our nanoribbons is likely to be around 0.5 μm at 2 K, consistent with an order-of-magnitude estimate from SdH measurements (Supplementary Fig. S4). Further experiments down to lower temperatures are expected to enhance L_ϕ for the observation of Aharonov–Bohm effects in wider ribbons and will be investigated in the future.

We have fabricated topological insulator materials in nanoribbon form, with large surface-to-volume ratios. We report the first transport measurement in this class of materials, on the basis of the Aharonov–Bohm oscillations of the conductance associated with the topological surface states. The distribution of the Aharonov–Bohm periods provides clear evidence to distinguish the surface conductance from the bulk, paving the way to eventually

eliminate the bulk conduction. Robust transport properties of the topological surface state enable new spintronics applications at room temperature.

Methods

Bi_2Se_3 nanoribbon synthesis. Single-crystalline Bi_2Se_3 nanoribbons were grown inside a 12 inch horizontal tube furnace (Lindberg/Blue M) equipped with a 1-inch-diameter quartz tube. The silicon ⟨100⟩ substrates were decorated with 20-nm-diameter Au nanoparticle catalysts, by functionalizing with 0.1% w/v aqueous poly-L-lysine solution (Ted Pella) and dipping into 20-nm-diameter Au colloid solution (Ted Pella). For Sn-doped Bi_2Se_3 nanoribbon synthesis, Sn/Au (5 nm Sn and 2 nm Au) double-layer alloy catalysts are used to introduce trace amounts of Sn to nanoribbons. The powder of Bi_2Se_3 (Alfa Aesar, Purity 99.999%) was placed in the hot centre region as the precursors for evaporation. Ultrapure argon was used as a carrier gas to transport the vapour to the colder furnace region. The silicon ⟨100⟩ substrates covered with catalysts were placed downstream at certain locations to accurately set the temperature. The tube was pumped to a base pressure of 30 mtorr and flushed with the carrier gas repeatedly to decrease oxygen contamination. The typical synthesis conditions for Bi_2Se_3 nanoribbons are: 0.2 g Bi_2Se_3, pressure 50 torr, source temperature 500 °C, duration time 5 h and carrier gas flow rate 120 s.c.c.m. Bi_2Se_3 nanoribbons grew preferentially at the position range of 6–10 cm away from the hot centre region of the furnace, where the temperature range was 420–480 °C.

Device fabrication. The Bi_2Se_3 nanoribbons were mechanically transferred from the growth substrate onto 150-nm-thick silicon nitride on p-Si ⟨100⟩ substrates restructured with a marker array for transport studies. Electron beam lithography was used to pattern electrodes onto individual nanoribbons by means of the markers. Electron-beam evaporating Ti/Au (5 nm Ti and 195 nm Au) is used as the contact metal, which we found to form ohmic contacts without any annealing.

Characterization. Characterization was done using SEM (FEI XL30 Sirion, acceleration voltage 5–30 kV), TEM (Philips CM20-FEG, acceleration voltage 200 kV) and AFM (Park Systems XE-70). Carbon film supported on copper or gold grids was used only for TEM characterization.

Transport measurements. Four-terminal current/voltage (I/V) measurements were carried out in a cryogenic probe station (Janis Research, ST-4LF-2X-1Y-CX) coupled to an Agilent B1500A semiconductor device analyser at room temperature. Low-frequency (1,000 Hz) and d.c. standard four-probe magnetoresistance measurements were carried out in a Quantum Design PPMS-7 instrument, Janis-9T magnet He-cryostats and a Keithley S110 Hall effect measurement system. The temperature range is 2–300 K and the magnetic field is up to ±9 T that applied for various orientations of the applied magnetic field with respect to the ribbon length.

Received 24 August 2009; accepted 23 November 2009; published online 13 December 2009

References

1. Bernevig, B. A., Hughes, T. L. & Zhang, S. C. Quantum spin Hall effect and topological phase transition in HgTe quantum wells. *Science* **314,** 1757–1761 (2006).
2. König, M. *et al.* Quantum spin hall insulator state in HgTe quantum wells. *Science* **318,** 766–770 (2007).
3. Zhang, H. *et al.* Topological insulators in Bi_2Se_3, Bi_2Te_3 and Sb_2Te_3 with a single Dirac cone on the surface. *Nature Phys.* **5,** 438–442 (2009).
4. Xia, Y. *et al.* Observation of a large-gap topological-insulator class with a single Dirac cone on the surface. *Nature Phys.* **5,** 398–402 (2009).
5. Fu, L., Kane, C. L. & Mele, E. J. Topological insulators in three dimensions. *Phys. Rev. Lett.* **98,** 106803 (2007).
6. Moore, J. E. & Balents, L. Topological invariants of time-reversal-invariant band structures. *Phys. Rev. B* **75,** 121306 (2007).
7. Qi, X. L., Hughes, T. L. & Zhang, S. C. Topological field theory of time-reversal invariant insulators. *Phys. Rev. B* **78,** 195424 (2008).
8. Chen, Y. L. *et al.* Experimental realization of a three-dimensional topological insulator, Bi_2Te_3. *Science* **325,** 178–181 (2009).
9. Taskin, A. A. & Ando, Y. Quantum oscillations in a topological insulator $Bi_{1-x}Sb_x$. *Phys. Rev. B* **80,** 085303 (2009).
10. Fu, L. & Kane, C. L. Topological insulators with inversion symmetry. *Phys. Rev. B* **76,** 045302 (2007).
11. Aharonov, Y. & Bohm, D. Significance of electromagnetic potentials in the quantum theory. *Phys. Rev.* **115,** 485–491 (1959).
12. Raghu, S., Chung, S. B., Qi, X. L. & Zhang, S. C. Collective modes of a helical liquid. Preprint at <http://arxiv.org/abs/0909.2477> (2009).
13. Bernevig, B. A. & Zhang, S. C. Quantum spin Hall effect. *Phys. Rev. Lett.* **96,** 106802 (2006).
14. Kane, C. L. & Mele, E. J. Quantum spin Hall effect in graphene. *Phys. Rev. Lett.* **95,** 226801 (2005).
15. Hsieh, D. *et al.* A topological Dirac insulator in a quantum spin Hall phase. *Nature* **452,** 970–974 (2008).
16. Mishra, S. K., Satpathy, S. & Jepsen, O. Electronic structure and thermoelectric properties of bismuth telluride and bismuth selenide. *J. Phys. Condens. Matter* **9,** 461–470 (1997).
17. Qi, X. L., Li, R. D., Zang, J. D. & Zhang, S. C. Inducing a magnetic monopole with topological surface states. *Science* **323,** 1184–1187 (2009).
18. Fu, L. & Kane, C. L. Superconducting proximity effect and majorana fermions at the surface of a topological insulator. *Phys. Rev. Lett.* **100,** 096407 (2008).
19. Ando, T., Fowler, A. B. & Stern, F. Electronic properties of two-dimensional systems. *Rev. Mod. Phys.* **54,** 437–672 (1982).
20. Aronov, A. G. & Sharvin, Y. V. Magnetic-flux effects in disordered conductors. *Rev. Mod. Phys.* **59,** 755–779 (1987).
21. Hyde, G. R., Beale, H. A., Spain, I. L. & Woollam, J. A. Electronic properties of Bi_2Se_3 crystals. *J. Phys. Chem. Solids* **35,** 1719–1728 (1974).
22. Morales, A. M. & Lieber, C. M. A laser ablation method for the synthesis of crystalline semiconductor nanowires. *Science* **279,** 208–211 (1998).
23. Wyckoff, R. W. G. *Crystal Structures* (Krieger, 1986).
24. Lee, P. A. & Stone, A. D. Universal conductance fluctuations in metals. *Phys. Rev. Lett.* **55,** 1622–1625 (1985).
25. Hikami, S., Larkin, A. I. & Nagaoka, Y. Spin–orbit interaction and magnetoresistance in the 2 dimensional random system. *Prog. Theor. Phys.* **63,** 707–710 (1980).
26. Huber, T. E., Celestine, K. & Graf, M. J. Magnetoquantum oscillations and confinement effects in arrays of 270-nm-diameter bismuth nanowires. *Phys. Rev. B* **67,** 245317 (2003).
27. Berggren, K. F., Thornton, T. J., Newson, D. J. & Pepper, M. Magnetic depopulation of 1D subbands in a narrow 2D electron gas in a GaAs:AlGaAs heterojunction. *Phys. Rev. Lett.* **57,** 1769–1772 (1986).
28. Altshuler, B. L., Aronov, A. G. & Spivak, B. Z. The Aharonov–Bohm effect in disordered conductors. *Jetp Lett.* **33,** 94–97 (1981).
29. Bachtold, A. *et al.* Aharonov–Bohm oscillations in carbon nanotubes. *Nature* **397,** 673–675 (1999).
30. Washburn, S., Umbach, C. P., Laibowitz, R. B. & Webb, R. A. Temperature dependence of the normal-metal Aharonov–Bohm effect. *Phys. Rev. B* **32,** 4789–4792 (1985).

Acknowledgements

We would like to thank D. Goldhaber-Gordon, K. A. Moler, J. Analytis and J. Maciejko for the helpful discussion. Y.C. acknowledges the support from the King Abdullah University of Science and Technology (KAUST) Investigator Award (No. KUS-l1-001-12). H.P. acknowledges the support from MOST (2007CB936203). K.L. acknowledges the KAUST Postdoctoral Fellowship support No. KUS-F1-033-02. Y.L.C. and Z.X.S. acknowledge the support from the Department of Energy, Office of Basic Energy Sciences under contract DE-AC02-76SF00515.

Author contributions

H.P., K.L. and Y.C. conceived and designed the experiments. H.P., D.K. and S.M. carried out the synthesis, structural characterization and device fabrication. K.L., H.P., S.M. and D.K. carried out the transport measurements and analyses. Y.L.C., and X.Q. assisted in experimental work and theoretical analysis. All authors contributed to the scientific planning and discussions. H.P., K.L., Z.X.S., S.C.Z. and Y.C. contributed to the preparation and discussion of the manuscript.

Additional information

The authors declare no competing financial interests. Supplementary information accompanies this paper on www.nature.com/naturematerials. Reprints and permissions information is available online at http://npg.nature.com/reprintsandpermissions. Correspondence and requests for materials should be addressed to Y.C.